TRANSPORT AND FATE OF NATURAL GAS AND BRINE ESCAPING FROM A HYDROCARBON RESERVOIR THROUGH A FAILED DEEP-WATER WELL IN THE OCEANIC SUBSURFACE OF THE GULF OF MEXICO

M.T. Reagan,[1,4], G.J. Moridis[1,2], N.D. Keen[1], Lee, K.J. [2],

M. Natter[3], T. Bjerstedt[3], and W.W. Shedd[3]

[1.] ***Energy Geosciences Division, Lawrence Berkeley National Laboratory, Berkeley, CA 94720.***

[2.] ***Department of Petroleum Engineering, Texas A&M University, College Station, TX 77843.***

[3.] ***Bureau of Ocean Energy Management, New Orleans, LA 70123.***

[4.] ***Corresponding author**: mtreagan@lbl.gov*

Acknowledgements

This work was carried out under Interagency Agreement M14PG00044 between the Bureau of Ocean Energy Management and Lawrence Berkeley National Laboratory. This research used resources of the National Energy Research Scientific Computing Center, a DOE Office of Science User Facility supported by the Office of Science of the U.S. Department of Energy under Contract No. DE-AC02-05CH11231.

Abstract

The possibility of broaching, or the release of fluids at the seafloor due to a damaged or faulty well, is a hazard that must be assessed in the well-permitting process. This paper describes a numerical simulation study of a real-life scenario where a complex, permeable sandy formation, connected to the seafloor via known chimneys/seeps, is intersected by a damaged production well that drains another deeper, gas-bearing formation. The objective of the study to determine the transport and fate of hydrocarbon reservoir fluids (gas and brines) escaping into the sandy formation through the casing shoe of the failed well, and to determine the time it takes for these contaminants to reach the ocean floor. We conducted a detailed simulation study to represent the conditions, properties, and behavior of the system under such failure conditions, and we investigated the migration of gas and brine for a range of reservoir and chimney properties. A key conclusion is that, for such complex systems, modeling the three-dimensional geometry of the system in detail is key to describing transport and assessing the time and magnitude of potential releases. For the system studied here, transport times range from under two years (highest permeabilities) to many decades, ensuring significant time to respond to potential broaching hazards. Under the conditions investigated in this study, we also determine that gas-dominated releases associated with low rates of water flow into the sandy formation are likely to cause hydrate formation that can reduce permeabilities in the colder, upper regions of the chimneys and possibly mitigate releases.

Keywords

Broaching, Hydrate Formation, Well Failure, Hazard Assessment, Reservoir Simulation

1. Introduction

Oil and gas production in the Gulf of Mexico often requires complex drilling technologies, including the use of directional drilling at great depths. Improperly constructed or damaged well casings could allow the escape of reservoir fluids into formations they intersect, creating the possibility of contaminant releases at the seafloor—a phenomenon referred to as broaching. The Bureau of Ocean Energy Management (BOEM) began performing broaching evaluations after the uncontrolled release of oil and gas from the Macondo reservoir in Mississippi Canyon Block 252 (Oldenburg et al., 2012). The sub-seafloor segments of the Macondo well had apparently maintained integrity and the well was eventually capped successfully. The Macondo study addressed the problem of well failure at the ocean floor, and as such could not provide answers to the question of how long it could take for broaching to occur after a well failure deeper in the oceanic subsurface. For scenarios where a well failure creates connectivity between a deep, over-pressured hydrocarbon reservoir and overlying permeable formations, there is no methodology to determine the fate and transport of the released fluids and whether broaching is a possibility. Hazard assessments must be performed to determine whether uncontrolled releases could be contained and stopped in time to prevent escape of hydrocarbons into the environment. For example, how much time would be available to drill a relief well before broaching occurs at the seafloor?

To answer some of these questions, BOEM completed an Interagency Agreement with the U.S. Department of Energy/Lawrence Berkeley National Laboratory to carry out 3D modeling of possible scenarios of reservoir fluid releases from compromised casing shoes in two real-life systems that had been qualitatively judged as either likely or possible to result in broaching. This paper describes the numerical simulation work for scenarios associated with the first system: a “supra-salt” system where a permeable formation, connected to the seafloor via known chimneys/seeps, is intersected by a damaged well producing from a deeper formation.

The system of interest involves a roughly 6 km x 10 km (3.7 x 6.2 mi) region of permeable sand (the Purple Sand) intersected by a well producing from a deeper, warmer, higher-pressure formation (Figure 1). The Purple Sand is flanked by two chimneys (Figure 2) that are considered permeable to fluids escaping from deeper hydrocarbon reservoirs in the Gulf of Mexico -- at least one of them has been confirmed to be a prolific hydrocarbon seep (Garcia-Pineda et al., 2010; Roberts et al., 2010). Portions of the Purple Sand formation climb updip from the potential casing-shoe failure point toward the two chimneys, both of which are confirmed active oil and gas seep sites. This suggests there are clear pathways for migration to the seafloor of fluids released into the Purple Sand. The seeps, seismic wipe out zones, and sea bottom seismic amplitude anomalies in association with them provide strong evidence for a leaky system (Figure 2).

The goal of the overall simulation study is to assess the potential transport of reservoir fluids through the Purple Sand and the possibility of the emergence of reservoir fluids (gas and brine in this case) at the seafloor if a permeable pathway is created between the deeper reservoir and the Purple Sand via a failure in the intersecting well. To accomplish this, we conducted a detailed simulation study that faithfully represented the conditions, properties, and behavior of the system under such a release.

2. Methodology

2.1 Mesh Generation and System Initialization

The effort to discretize the domain for the simulation effort included two different sets of grids. The first set was that of the elevation grids and included elevation data (from the dataset represented by Figure 2) to the top of the Purple Sand on a regular pattern (ranging in spacing from 150 ft x150 ft to 50 ft x50 ft). The elevation grids served as the basis for the development of the simulation grids, i.e., the element system used by the pTOUGH+HYDRATE simulations (Moridis et al., 2008; Zhang et al., 2008; Moridis, 2014). Unlike the elevation grids, the simulation grids (which were developed by the LBNL team) were irregular in the element size, providing higher definition in the vicinity of important features and a coarser discretization at locations that did not appear to play key roles in the fluid transport (as determined and confirmed by scoping simulations).

BOEM provided mapped data from 3D depth migrated seismic showing the geometry of the geosystem over multiple Outer Continental Shelf (OCS) blocks. Mapped data was interpreted on a GeoFrame workstation using U.S. feet in Universal Transverse Mercator (UTM) 15 projection. Mapped surfaces on the top of salt and on the top of the Purple Sand and 3D seismic arbitrary lines provided the system geometry, and GIS shape files of sea floor features and seismic amplitude were available for overposting. The mechanical and formation fluid properties for the Purple Sand were obtained from well logs by BOEM staff using Log Evaluation System Analysis software.

The extreme thinness of the Purple Sand carrier bed compared to the lateral dimensions of this formation, the very large height of the chimneys, the undulations of the sand, and the steepness of the elevation gradient near the base of the chimneys, coupled with the need to integrate a flow pathway to each seep site resulted in frequent vertical discontinuities using conventional TOUGH+ mesh generation methods. The MeshMaker 2.0 (MM2) gridding software (Moridis and Keen, 2015; Moridis, 2016) was developed specifically to address the challenges of this system geometry. MM2 uses the elevations of the top of the formation over its footprint (using data provided in tabular form) and powerful 3D interpolation algorithms to create grids that can conform to practically any irregular geometry. The new grids created by MM2 eliminated a common continuity problem in undulating surfaces by incorporating directional slopes and correct volumes and surface areas into elements describing those surfaces. MM2 thus allows irregular meshes to represent complex surfaces, while still providing the numerical stability afforded by meshes of pure “stacked bricks” without the distortions that such configurations impose on fluid flow.

Several realizations of various grid refinement levels were constructed following the process described above, including up to 6.7M gridblocks. After comparisons of the 3D images of the grids (in an effort to determine which iteration captured key geometric features of the system) and of the corresponding execution times, a grid involving 2.65M gridblocks (Figure 3) was selected as the most appropriate for the simulations because it reproduced with high fidelity the system geometry while requiring reasonable (relatively-speaking) execution times.

The final 3D system, with 2,647,145 gridblocks, was brought to a physically correct initial state via numerical simulation, using as fixed reference points the pressures corresponding to the seafloor depths at the tops of the two chimneys and temperatures at the seafloor, as well as a representative “average” sub-seafloor temperature gradient (see Table 1). A long-term simulation then calculated the hydrostatic pressure field and the equilibrium temperature profile for the given sediment properties. For systems that lie within the zone of hydrate stability (and thus have a potential for hydrate occurrence or hydrate formation if methane becomes available at the location under investigation), this is the only physically correct and consistent way to establish an initial condition. The results of this simulation provided stable initial conditions for subsequent fluid release modeling.

The initial conditions included:

- A hydrostatic pressure distribution in the entire 3D domain (Purple Sand and chimneys,
- A specified average temperature gradient from the BOEM dataset: 2.71°C/100m, with an estimated seafloor temperature of 3.9°C at the seafloor (Gallaway et al., 2001; Forrest et al., 2007),
- An assumption of 1 ppm background methane in the aqueous phase. This was a reasonable assumption (given the lack of information on the subject), and has no impact even if it is incorrect because (a) methane solubility in water is very low and (b) dissolved gas is overwhelmed when gas from the reservoir is released either as free gas.

The physical parameters used were supplied by BOEM, or selected under consultation with BOEM, and are given in Table 2 and Table 3. Figures 3 and 4 show the mesh connectivity and the initial pressure distribution at the various components of this 2.6M-element system viewed from different angles. In Figure 3, an overall view of the system (view at an angle, from above), shows the extensive but thin Purple Sand, with the two chimneys, A and B, reaching upward to the seafloor. Note that impermeable sediments, represented as heat-transfer boundaries, are not shown in this or any other rendering—only permeable formations are visualized. Figure 4 shows a rotated view of the system, with a close-up of Chimney B and its mesh connectivity. These visualizations of the simulation mesh will be used later in this paper to render the water and gas distributions in the failure scenarios. Visualizations were performed using the tough-convert postprocessor (Queiruga, 2018).

2.2 Reservoir Simulation

Following mesh creation and system equilibration, we conducted a set of simulations describing several scenarios of casing-shoe failure. We varied the permeability of the sand and chimneys to assess the basic sensitivity to system properties. Because of lack of information on its properties (and a conservative approach), the fault near the base of the Chimney A was treated as a permeable feature, and the elevation offset was described using steeply angled but connected gridblocks. In the spirit of the “worst-possible scenario”, this approach allowed the fastest possible upward flow toward the chimney.

For each release scenario, constant-pressure and temperature conditions were imposed at the casing shoe failure point. These were the conditions in the connecting reservoir, without any adjustment for the elevation differences between the reservoir and the casing shoe: P = 51 MPa and T = 63.3^{o}C . Because the pressure and temperature drops in the failed well could not be estimated, this conservative approach was followed. The gas saturation at the failure point was initially S_G = 0.99, with an alternative case of S_G = 0.89 used to study the effects of water release in concert with gas release. The point of leakage was also given the properties of an open well, a pseudo-medium with $\varphi = 1$, a high $k = 5 \times 10^{-9}$ m^2, a capillary pressure $P_c = 0$, a relative permeability that was a linear function of the phase saturations in the wellbore, and a low (but nonzero) irreducible gas saturation $S_{irG} = 0.005$. Simulations were run to a maximum duration of 100 years, or until a logical stopping point was reached, e.g., gas and brine broaching at one or both chimneys. During the simulations, we monitored the flow of fluids through the tops of the chimneys and monitored *T* and *P* conditions at selected points within the chimneys and in the Purple Sand.

The parametric variations used for the sensitivity study were:

Released Gas Saturation, S_G:	0.89, 0.99, with corresponding aqueous saturations S_A = 0.11 and 0.01, respectively
Chimney Permeability, k_C:	k_C = 541 mD, 100 mD, 1000 mD for k_S = 541 mD
Sand Permeability, k_S:	k_S = 541 mD, 100 mD, 1000 mD for k_C = 541 mD

Simulation runs were performed using the pTOUGH+HYDRATE parallel code (Zhang et al., 2008), an MPI parallel version of the TOUGH+HYDRATE (T+H) code. T+H can model all the known processes involved in the system response of natural CH_4-hydrates in complex geologic media (Moridis et al., 2014; Moridis and Pruess, 2014). T+H is a fully compositional simulator, descended directly from the TOUGH family of codes (Pruess, 2003), and it accounts for heat and up to four mass components (i.e., H_2O, CH_4, CH_4-hydrate, and water-soluble inhibitors such as salts) that are partitioned among four possible phases (gas, aqueous liquid, ice, and hydrate). It can describe 15 possible thermodynamic states (phase combinations) of the CH_4+H_2O system and can handle the phase changes, state transitions, strong nonlinearities, and sharp fronts that are typical of hydrate dissociation problems. Runs were performed on NERSC Edison and Cori I, and LBNL's Lawrencium LR3 and LR4 using 384 to 4,096 processors and a total of about 1.1 million CPU-hours.

3. Results

3.1. All-Gas Reference Case (k_c = k_s = 541 mD)

Water and Gas Flows. Figure 5 shows the total upward gas and water flows at the seafloor through the top of Chimney A and Chimney B (flows through A and B were summed in pT+H to give an estimate of the total flow through both chimneys). As gas first approaches the seafloor, upward water flow increases, driven by buoyant gas rise within Chimney B. The gas first reaches the top of Chimney B, where the gas breakthrough at the seafloor begins at t = 926 d. Gas escapes continuously from the top of Chimney B until an abrupt cessation of gas escape at t = 1,287 d. Total water flows decrease during the initial period of gas release, reaching a local minimum just before the cessation of the gas release. Visualizations of the simulation results (shown in the next section) indicate that 100% of the gas release occurs at Chimney B for $t \leq$ 1,287 d. Water flows increase gradually until t = 1,959 d, at which point gas release begins at Chimney A. The simulation was halted after 2,000 d. Water flows decrease once gas appears at the top of Chimney B.

Hydrate formation. The cessation of gas flow and the reduction of water flows are explained by the formation of hydrate near the summit of Chimney B. Figure 6 shows the total system-wide rate of hydrate formation vs. time for the entire simulation. Hydrate begins to form at t = 840 d, just before gas begins to escape into the ocean from the top of Chimney B. As shown by the visualization of the simulation results, this hydrate formation occurs entirely in Chimney B when the rising released gas arrives at depths with appropriately low temperatures for hydrate formation to occur. Hydrate formation continues as gas escapes from Chimney B at the seafloor, and proceeds at varying rates (as affected by changing temperature, pressure and salinity at the locations where hydrates form). Thus, the rate of hydrate formation Q_H reaches a first peak at about t = 926 d, and attains a maximum rate at about at t = 1,450 d. The period from t = 920 d to 1,200 d corresponds to the period of gas release at the seafloor. A column of rising gas forms a “tunnel” of solid, low-permeability hydrate with a permeable core, as coupled flow, thermal and phase behavior processes temporarily allow an open channel for gas to flow even as hydrate accumulates in the surrounding chimney sediments. As the hydrate saturations increase, the effective permeability of Chimney B decreases. Eventually, the effective permeability in the chimney drops to zero when hydrate saturations exceed 80%. When this occurs at about t = 1,287 d, the top of Chimney B is effectively blocked, and the hydrate formation rate increases as gas rising in the chimney is trapped below an impermeable layer of hydrate.

System-wide hydrate formation rates begin to increase again at t = 1,900 d, and this increase is associated with gas moving upward in Chimney A and encountering suitable pressures and temperatures for hydrate formation and stability. The decline in the corresponding water flow rates that are evident in Figure 5 are associated with hydrate formation in Chimney A and the resulting reduction in permeability. Continuation of gas flow and hydrate formation in Chimney A is expected to lead eventually to complete blockage to flow (as is the case in Chimney B).

Figure 7 shows the cumulative hydrate mass formed within the entire simulated domain. We can identify the onset of hydrate formation in Chimney B at t = 840 d, the formation of hundreds of millions of kilograms of hydrate over the course of 1,200 d, and also the upward inflection in the cumulative curve at t = 1,900 d when hydrate begins forming in Chimney A.

Visualizations. New 3-D visualization capabilities, developed in the course of the overall project, allow detailed tracking of gas plumes across the simulation domain. For this simulation case, the visualizations are renderings of mesh connectivity (each connection between elements as a line segment) as previously shown in Figures 3 and 4, with the gas and/or the hydrate saturations mapped onto the line segments via color scales. This allows some limited transparency in the visualization, helping to better represent the movement of gas within the thin body of the Purple Sand and along the sides of the chimneys.

Figure 8 shows the evolution of gas saturation with a view directed toward Chimney B at selected simulation times. The intersection of the failed well with the Purple Sand layer is at the lower left corner of the domain. At t = 180 d and t = 640 d, the escaping gas expands outward from the point of the casing shoe failure, and is seen to preferentially move toward Chimney B (upper left). At t = 870 d, the gas has already reached Chimney B, and is seen rising (primarily by buoyancy, although there is some pressure differential and upward flow of water) through the side of the chimney facing the leak. The panel at t = 1,000 d depicts the phase saturation distributions just after gas reaches the seafloor (i.e., the boundary at the top of Chimney B). At this point, the permeability at the top of the chimney begins to decrease because of hydrate formation. The panel at t = 1,360 d provides a snapshot of the system just after the cessation of the flows of gas and water to the seafloor through the top of Chimney B, with the gas saturation at the top of the chimney showing evidence of uniformity—essentially the plugged chimney is now filling up with gas rising from below. The last frame, at t = 2,000 d, shows a chimney with the upper several hundred meters filled with gas saturations $S_G \geq 0.50$.

The advance of gas toward, and release through, Chimney A is illustrated by the four frames in Figure 9. At t = 60 d and t = 1,280 d, the gas is seen moving in a broad front toward the chimney. By t = 1,730 d, the topographical characteristics of the Purple Sand cause the front to split into two plumes moving toward Chimney A, one heading upslope along the upthrown footwall of the fault to the chimney on the left, and one heading upslope along the downthrown hanging wall of the fault. By t = 1,910, the gas has reached Chimney A through both pathways, a lower entry point near the downthrown hanging wall to the right and through a more tortuous path over the upthrown footwall to the left. Breakthrough, or broaching, at the seafloor occurs soon after, as gas rises to the top of the chimney via buoyancy and pressure gradients.

The evolution of hydrate saturation in Chimney B is illustrated by the four frames in Figure 10. At t = 910 d, hydrate appears along the side of the chimney as the rising gas deposits the first layers of solid hydrate. By t = 1,090 d, hydrate formation has reached the seafloor, and saturations increase rapidly near the top of the chimney, with a corresponding reduction in permeability. The frame for t = 1,280 d depicts the hydrate saturation distribution just as water and gas flows out of the chimney have ceased. At that time and beyond, gas accumulating in the chimney leads to hydrate formation at successively lower elevations within the chimney (in parallel with the accumulation of gas in those regions, see Figure 8). At t = 2,000 d, hydrate deposits at saturations of $S_H \geq 0.50$ are extensive throughout Chimney B even at elevations hundreds of meters below the seafloor, creating permeability barriers to upward flow.

3.2. Sensitivity to Permeabilities.

To assess the complex variation in breakthough times (at the seafloor), multiple full simulations of the broached system were conducted using identical initial conditions, but higher or lower permeabilities for the Purple Sand and for the chimney media. The range of permeabilities included:

Chimney Permeability, k_c:	k_c = 100 mD, k_c = 541 mD, k_c = 1000 mD for k_s = 541 mD
Sand Permeability, k_s:	k_s = 100 mD, k_s = 541 mD, k_s = 1000 mD for k_c = 541 mD

For the sensitivity simulations, simulation length was limited to the point of gas breakthrough at the seafloor, as dictated by the need to efficiently utilize limited supercomputer CPU time. For these sensitivity simulations, we did not conduct a full analysis of hydrate formation and permeability reduction because we expected similar behavior for all cases that exhibit breakthroughs. The breakthrough curves for the permeability cases listed above are found in Figure 11.

As would be expected, lower-permeability features result in longer times until release at the ocean floor. Decreasing the chimney permeability by a factor of five results in a 60% longer breakthrough time (625 days) for gas to appear at the seafloor. Doubling the chimney permeability, however, results in only a slightly faster appearance of gas at the seafloor (by 64 days only, probably because of the rapid rise of the buoyant gas in the limited vertical dimension of the chimney). Decreasing permeability of the Purple Sand to 100 mD, however, has, unsurprisingly, a large effect—gas takes 3.5X longer (3,858 days) to emerge at the ocean floor. Doubling the sand permeability, conversely, only shifts the gas breakthrough forward by 309 days (617 days).

Plots of the arrival times at the seafloor (solid lines) and of the arrival times at the base of chimney B (dotted line) are presented in Figure 12, which shows the significantly non-linear dependence of these times on the permeabilities of the various components of the system. The red curve gives arrival times at the seafloor for k_s = 541 mD and k_c values of 100, 541 (base), and 1000 mD. The blue curve shows arrival times at the seafloor for k_c = 541 mD, and k_s values of 100, 541 (base), and 1000 mD. Figure 12 also shows arrival times at the base of chimney B (first gas exiting the Purple Sand) for k_{sand} values of 100, 541, and 1000 mD with $k_{chimney}$ = 541 mD (arrival times at the chimney did not vary significantly with $k_{chimney}$).

To help with hazard assessment, parametric expressions were created to estimate arrival time for a range of permeabilities. A series of curve fits was used in an attempt to represent the limited data points as a larger response surface. Various functional forms (polynomial, power laws) were tested, and the resulting curves were selected for convenience and ease-of-use. Although the system is very complex (and strongly dependent on the specific geometry of the sand in particular), it is reasonable to expect the arrival times to vary smoothly and gradually with respect to permeabilities. Thus, the curves generated through fits to an exponential form gave the only smoothly varying representation.

After fitting the data within Igor Pro (our data analysis and plotting environment), we generated the following equations:

Equation (1) estimates the arrival time at chimney B for varying Purple Sand permeabilities.

$$t_{chimney} = 418.62 + 4814.5 \exp\left(-5.2184 \times 10^{-3} k_s\right) \quad \ldots\ldots\ldots\ldots\ldots\ldots\ldots\ldots\ldots..(1)$$

Equation (2) estimates the arrival time at the seafloor for varying chimney permeabilities when k_s = 541 mD.

$$t_{seafloor} = 855.51 + 1171.9 \exp\left(-5.1974 \times 10^{-3} k_c\right) \quad \ldots\ldots\ldots\ldots\ldots\ldots\ldots\ldots (2)$$

Equation (3) estimates the arrival time at the seafloor for varying Purple Sand permeabilities when k_c = 541 mD.

$$t_{seafloor} = 584.77 + 5506.6 \exp\left(-5.1407 \times 10^{-3} k_s\right) \quad \ldots\ldots\ldots\ldots\ldots\ldots\ldots\ldots\ldots.(3)$$

These single-parameter variations can be expanded to a multiparameter surface. However, one additional detail that must be included is that the transit times through the chimneys, while largely a function of chimney permeability, will also vary slightly due to Purple Sand permeability. Differences in permeability may cause a different quantity of gas to arrive, or to arrive at a slightly different location. Additionally, attenuation via hydrate formation may change transit times. Consequently, a general equation for estimating breakthrough must include time-to-chimney, $t_{chimney}(k_s)$ and both $t_{chimney\text{-}seafloor}(k_c)$, and $t_{chimney\text{-}seafloor}(k_s)$. Calculated chimney transit times and the variation in transit times due to the effect of k_s are shown in Figure 13.

Now we can construct a parameterization of broaching time as:

$$t_{seafloor}(k_S, k_C) = t_{chimney}(k_S) + t_{chimney-seafloor}(k_C) + t_{difference}(k_S) \quad \ldots\ldots\ldots\ldots(4)$$

where

$$t_{difference}(k_S) = t_{chimney-seafloor}(k_S) - t_{chimney-seafloor}(k_C = 541\, mD) \quad \ldots\ldots\ldots(5)$$

Fitting each of the three terms to exponentials results in the following parametric expression:

$$t_{seafloor}(k_S, k_C) = 513.95 + 4814.5 \exp\left(-5.2184 \times 10^{-3} k_S\right) + 1172.9 \exp\left(-5.1974 \times 10^{-3} k_C\right) + 696.78 \exp\left(-4.6773 \times 10^{-3} k_S\right) \quad \ldots\ldots(6)$$

A visualization of the 3D surface associated with Equation (6) is given in Figure 14.

Note that these estimates are entirely a function of the specific (complex) geometry of the Purple Sand (and, to a lesser extent, of the chimneys), as represented in the model. For a system of this complexity, the gas arrival times at various locations of interest in the domain are strongly dependent on the accuracy of the 3D model. Heuristics that attempt to generalize to other (even similar) systems are not likely to be accurate. Note that the potential for hydrate formation and permeability reduction must be considered in any analysis of similar systems.

3.3. Water and Gas Release

Water and Gas Flows. Preliminary data provided by BOEM suggested a water saturation of approximately 11% within the underlying reservoir. As this is somewhat larger than the irreducible saturation of the Purple Sand, we considered an additional gas-release case where the released fluids included 11% water (likely an upper limit for water release). All other initial conditions were equal to the previous case.

The water-gas case exhibits drastically lower release rates at the shoe failure point, and much longer timeframes for gas migration. Figure 15 gives water and gas flow rates and cumulative release at the point of the leak vs. time. After an initial surge for $t < 1$ d, the release rates drop rapidly and eventually settle at a low rate of 0.03 m^3/s of gas and 19 kg/s for water. This is because of relative permeability effects, limited pressure gradients and weak buoyancy (as the density difference between the released brine and the native water is small).

Monitoring points within the Purple Sand (a point opposite the broach) and points in the center of each chimney tracked evolving conditions during the course of the release (Figure 16). We observe sharp increases in temperature within the chimneys after a few hundred days of leakage. This is caused by the constant flow of the warmer water into the system, and the temperature increases are attributed to both the temperature of the leaking water (63.3 ºC) and the fact that warmer water from deeper parts of the Purple Sand is swept upward toward the seafloor. As a results, the simulation was run for an additional 30 yr, to t = 100 yr, and yet no hydrate formation occurs anywhere in the system.

Visualizations. Visualizations of the evolving system are shown in Figure 17. At t = 4 yr, the expanding plume of gas moves away from the failure point, but much slower than in the all-gas case (Figures 8 and 9). By t = 25 yr, the plume has separated into two lobes, each heading toward each of the chimneys via the local high point (saddle) in the Purple Sand that connects the bases of the chimneys. Gas reaches the base of the chimneys at t = 41 yr, and reaches the seafloor at *both* chimneys at t = 70 yr. Careful examination of the visualizations shows the appearance of gas throughout and Purple Sand, and in areas away from the main plume as well, after t = 41 yr. This is caused by exsolution of dissolved gas from the aqueous phase due to the temperature increases as warmer water moves outward and upward from the release point at the casing shoe.

To track the movement of the water front, Figure 18 visualizes the salinity of the pore water over the same time intervals as seen in Figure 17. To create a natural tracer, the reservoir water entering at the failed casing shoe was given a concentration of 3.6wt% vs. 3.5wt% for water in the Purple Sand at the initial condition. This allows clear visualization of the water front. Compared to the narrow plumes of gas seen moving along the high points of the Purple Sand topography, the water front expands outward uniformly (because of favorable relative permeability conditions and very small density differences with the native water), initially outpacing the released gas at t = 4 yr and 25 yr. The more saline water enters the chimneys roughly at the same time as the gas at $t = 41$ yr, and reaches the seafloor at $t = 70$ yr. However, by this time the reservoir brine has largely displaced most of the water in the Purple Sand.

The most important conclusion from this alternative scenario is that the release of water with the gas shifts the timeframe for potential broaching from a few years to several decades. Release of water also adds heat (and, if the reservoir fluids are even more saline, an inhibitor) and prevents the formation of hydrate at the tops of the chimneys. Release rates are thus much smaller, broaching is delayed significantly, but the mitigating effects of hydrate formation will not be a factor.

4. Conclusions

The key conclusion from this investigation is that, for a system as complex as the Purple Sand/Chimney system, the three-dimensional geometry of the system is key to assessing the time and magnitude of releases. Any release pathway will have a length determined by a potentially tortuous gas or water pathway dependent on the topography of the sand body. The volume of this pathway will be dependent on the thickness of the sand. Changes in the geometry or topography, changes in connectivity between features, and any known heterogeneity must be included in a detailed and realistic model. Multiple release pathways between the shoe failure point and the chimneys may form depending on the contours of the permeability zone or zones. The multiphase flow regime (proportion of gas/water released) will also affect release rate, release travel time, and also alter the shape and length of the release pathway. All of these factors must be considered in hazard assessments. For this particular scenario, we expect timeframes from two years to many decades between casing shoe failure and potential broaching, depending on system permeabilities and the composition of the release. It is thus likely that there would be sufficient time to drill a relief well and control fluid releases before broaching of hydrocarbons at the sea floor could occur.

Once the geometries are established, parametric variations within those geometries result in fairly straightforward changes in expected travel times, with the unsurprising conclusion that the permeability of the pathway will greatly control the release timeline. Relative permeability effects related to the composition of the release would have even greater consequences, reducing leakage rates at the well and delaying releases at the seafloor. Alterations of the estimated thickness of the Purple Sand would likely have similarly large effects.

For systems with gas release and low rates of water injection into the system (water flow limited to displacement by the gas phase) it is likely that hydrate formation will reduce permeabilities in the colder, upper regions of the system and possibly mitigate release under the conditions seen in the simulations. One question that we cannot address at this point is how a system with all outlets blocked by hydrate would eventually behave if releases continued for longer periods of time.

5. References

Forrest, J., E. Marcucci and P. Scott, Geothermal Gradients and Subsurface Temperatures in the Northern Gulf of Mexico, Search and Discovery Article #30048, 2007, adapted from paper published in GCAGS Transactions, **55**, 233-248, 2005

Gallaway, B.J., J.G. Cole and L.R. Martin, The Deep Sea Gulf of Mexico : An Overview and Guide, OCS Study MMS 2001-065, U.S. Department of the Interior, Minerals Management Service, Gulf of Mexico OCS Region, 2001

Garcia-Pineda, O., MacDonald, I., Zimmer, B., Shedd, B., Roberts, H., Remote-sensing evaluation of geophysical anomaly sites in the outer continental slope, northern Gulf of Mexico. Deep Sea Research Part II: Topical Studies in Oceanography 57, 1859-1869, 2010

Moridis, G.J., User’s Manual for the HYDRATE V1.5 Option of TOUGH+ V1.5: A Code for the Simulation of System Behavior in Hydrate-Bearing Geologic Media, Report LBNL-6869E, Lawrence Berkeley National Laboratory, Berkeley, CA, 2014, *https://pubarchive.lbl.gov/islandora/object/ir%3A1005569*

Moridis, G.J., and Reagan, M.T. Gas Production From Oceanic Class 2 Hydrate Accumulations, *OTC 18866*, 2007 Offshore Technology Conference, Houston, Texas, U.S.A., 30 April–3 May 2007.

Moridis, G.J., User’s Manual of the MeshMaker V1.5 Code: A Mesh Generator for Domain Discretization in Simulations of the TOUGH+ and TOUGH2 Families of Codes, Report LBNL-1005134, Lawrence Berkeley National Laboratory, Berkeley, CA, 2016

Moridis, G.J. and K. Pruess, User’s Manual of the TOUGH+ v1.5 Core Code: A General Purpose Simulator of Non-Isothermal Flow and Transport Through Porous and Fractured Media, Lawrence Berkeley National Laboratory Report LBNL-6869E, August 2014, *https://pubarchive.lbl.gov/islandora/object/ir%3A1005566.*

Moridis, G.J. and N. Keen, MeshMaker V2.0S And V2.0P: New Grid Generators For Complex Heterogeneous Domains in TOUGH2/TOUGH+ Simulations, Proceedings, TOUGH

Symposium 2015, Lawrence Berkeley National Laboratory, Berkeley, California, September 28-30, 2015

Moridis, G.J., Kowalsky, M.B., Pruess, K., TOUGH+HYDRATE v1.0 User’s Manual: A Code for the Simulation of System Behavior in Hydrate-Bearing Geologic Media, Report LBNL-0149E, Lawrence Berkeley National Laboratory, Berkeley, CA, 2008.

Lawrence Livermore National Laboratory (LLNL), VisIt User’s Manual, Version 1.5, Report UCRL-SM-220449, 2005.

Oldenburg, C.M., Freifeld, B.M., Pruess, K., Pan, L., Finsterle, S., Moridis, G.J., Numerical simulations of the Macondo well blowout reveal strong control of oil flow by reservoir permeability and exsolution of gas, PNAS, 109 (50), 20254-20259, 2012.

Pruess, K., 2003. The TOUGH Codes – A Family of Simulation Tools for Multiphase Flow and Transport Processes in Permeable Media, LBNL Report 53630, *https://pubarchive.lbl.gov/islandora/object/ir%3A121930.*

Queiruga, A.F. and M.T. Reagan. (2018, February 2). tough_convert: Version 1.0. Zenodo. http://doi.org/10.5281/zenodo.1164418

Roberts, H.H., Feng, D., and Joye, S.B. Cold-seep carbonates of the middle and lower continental slope, northern Gulf of Mexico. Deep sea research part II: Topical Studies in Oceanography, 57(21), 2040-2054, 2010.

vanGenuchten, M.Th., A Closed-Form Equation for Predicting the Hydraulic Conductivity of Unsaturated Soils, Soil Sci. Soc., **44**, 892 - 898, 1980

Zhang, K., G.J. Moridis, Y.S. Wu and K. Pruess, A Domain Decomposition Approach For Large-Scale Simulations Of Flow Processes In Hydrate-Bearing Geologic Media. Proceedings of the 6th International Conference on Gas Hydrates (ICGH 2008), Vancouver, British Columbia, Canada, July 6-10, 2008

Table 1: Reservoir Properties Summary

Properties of Sand Layer and Chimneys			
Location	Parameters	Value	Unit
General	Geothermal gradient	0.0271	ºC/m
	Temperature at ocean floor	3.9(*)	ºC
	Porosity:		
	Average	0.25	fraction
	Low	0.1	fraction
	High	0.33	fraction
Purple Sand	Permeability:		
	Average	541/5.3E-13	mD/m^2
	Low	0.7/7.0E-16	mD/m^2
	High	1416/1.41E-12	mD/m^2
	Thickness	10/3	Ft/m
	Temperature (3,020 m)	127/52.8	ºF/ºC
	Well (x,y,z) at Purple Sand		
	x	9659.42	m
	y	4050.77	m
	z	-3136.39	m
Chimneys	Porosity	Same as Purple Sand	
	Permeability	Same as Purple Sand	
	Depth at ocean floor:		
	Chimney A	-1,135.38	m
	Chimney B	-1,181.10	m
Casing shoe	(x,y,z) of casing shoe		
	x	9799.3	m
	y	3810.0	m
	z	-2915.1	m
Escaping Fluids	P	7385	Psi
	T	146/63.3	ºF/ºC
	x_{CH4}	100	%

(*) Gallaway et al., 2001; Forrest et al., 2007

Table 2. Reservoir parameters

Region	k (mD)	ϕ	S_H	S_W
0. Boundary Layers	0	0.0	0.0	1.0
1. Chimney A	541	0.25	0.0	1.0
2. Chimney B	541	0.25	0.0	1.0
3. Purple Sand	541	0.25	0.0	0.0
4. Failed Well Casing	500-5000	1.0	0.0	varies

Table 3. Other simulation parameters.

Water salinity (mass fraction)	0.035
Grain density ρ_R (all formations)	2600 kg/m^3
Dry thermal conductivity k_{QRD} (all formations)	0.5 W/m/K*
Wet thermal conductivity k_{QRW} (all formations)	3.1 W/m/K*
Composite thermal conductivity model (Moridis et al., 2008)	$k_C = k_D + (S_A^{1/2}+S_H^{1/2})\ (k_W - k_D) + \phi\ S_I\ k_I$
Capillary pressure model (van-Genuchten, 1980; Moridis et al., 2008)	$P_{cap} = -P_0\left[\left(S^*\right)^{-1/\lambda}-1\right]^{(1-\lambda)}$ $S^* = \frac{(S_A - S_{irA})}{(S_{mxA} - S_{irA})}$
S_{irA}	0.24
	0.6
$1/P_0$	5.3x10^{-5} Pa^{-1}
3-Phase (Aqueous-Gas-Hydrate) Relative Permeability Model (Moridis et al., 2008)	$k_{rA} = (S_A*)^n$ $k_{rG} = (S_G*)^n$ $S_A*=(S_A-S_{irA})/(1-S_{irA})$ $S_G*=(S_G-S_{irG})/(1-S_{irA})$ OPM model (Moridis et al., 2008)
n	3.0
S_{irG}	0.02
S_{irA}	0.25

(*) Moridis and Reagan, 2007.

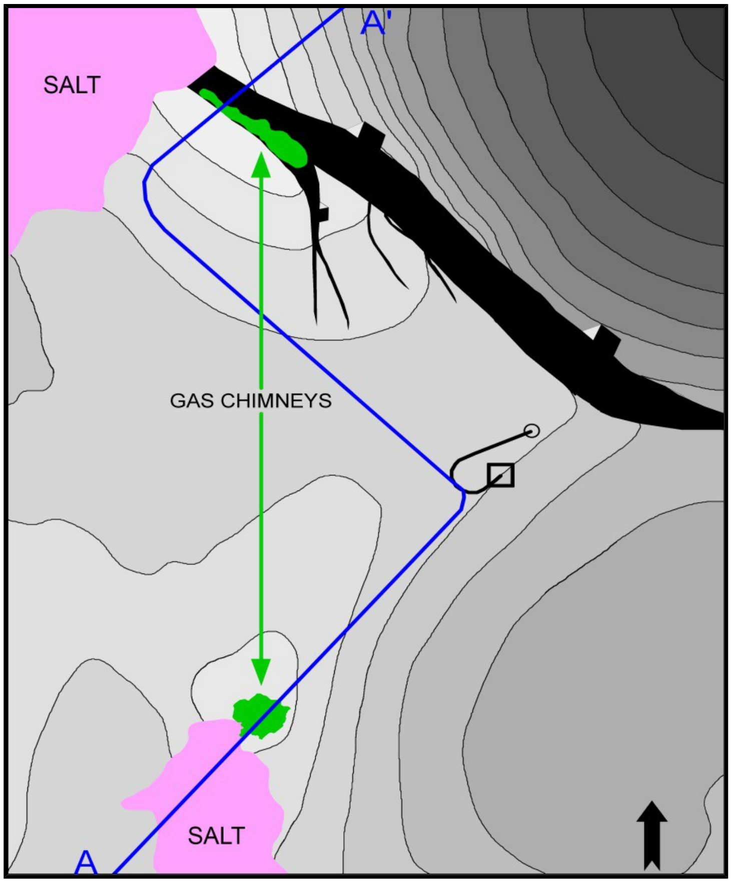

Figure 1. Structure map on the purple sand showing relative depth subsurface) in grey-shade, gas chimney locations, and seismic traverse A-A'. The well surface location is designated by a square and the bottom-hole location is designated by a circle (proprietary data courtesy of Western Geco/Schlumberger).

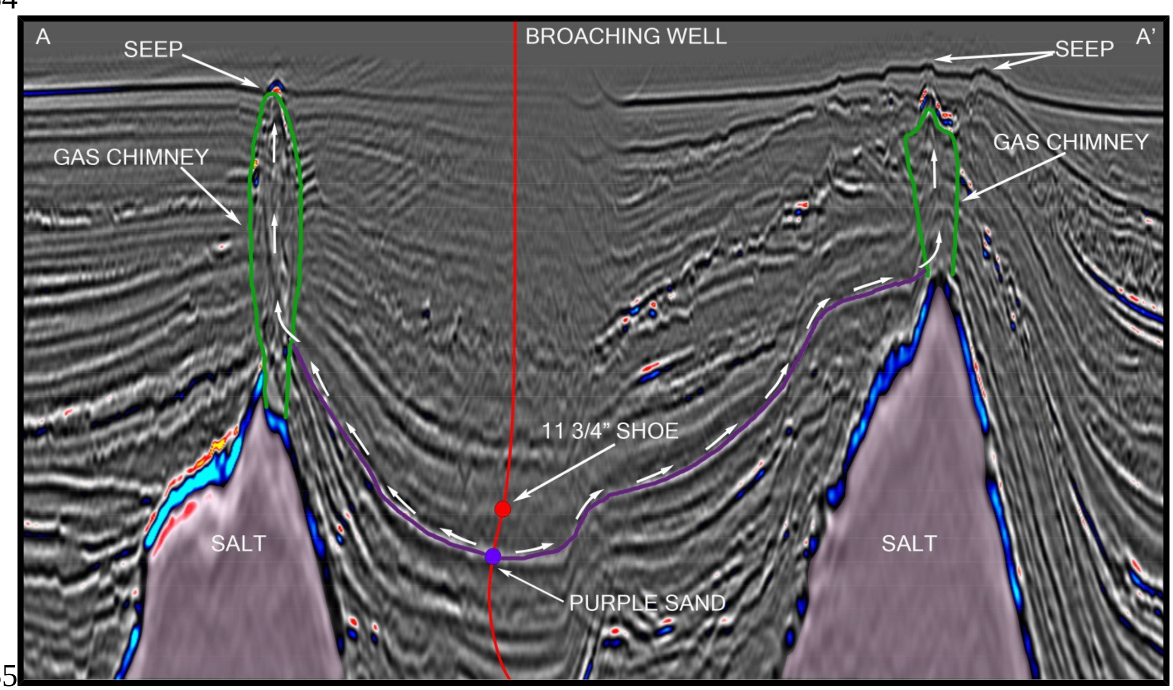

Figure 2. Purple sand seismic traverse A-A’ that shows well path, 11.75-in casing shoe, purple sand, broaching pathways, adjacent salt structures, natural seeps, and gas chimneys (proprietary seismic courtesy of WesternGeco, LLC).

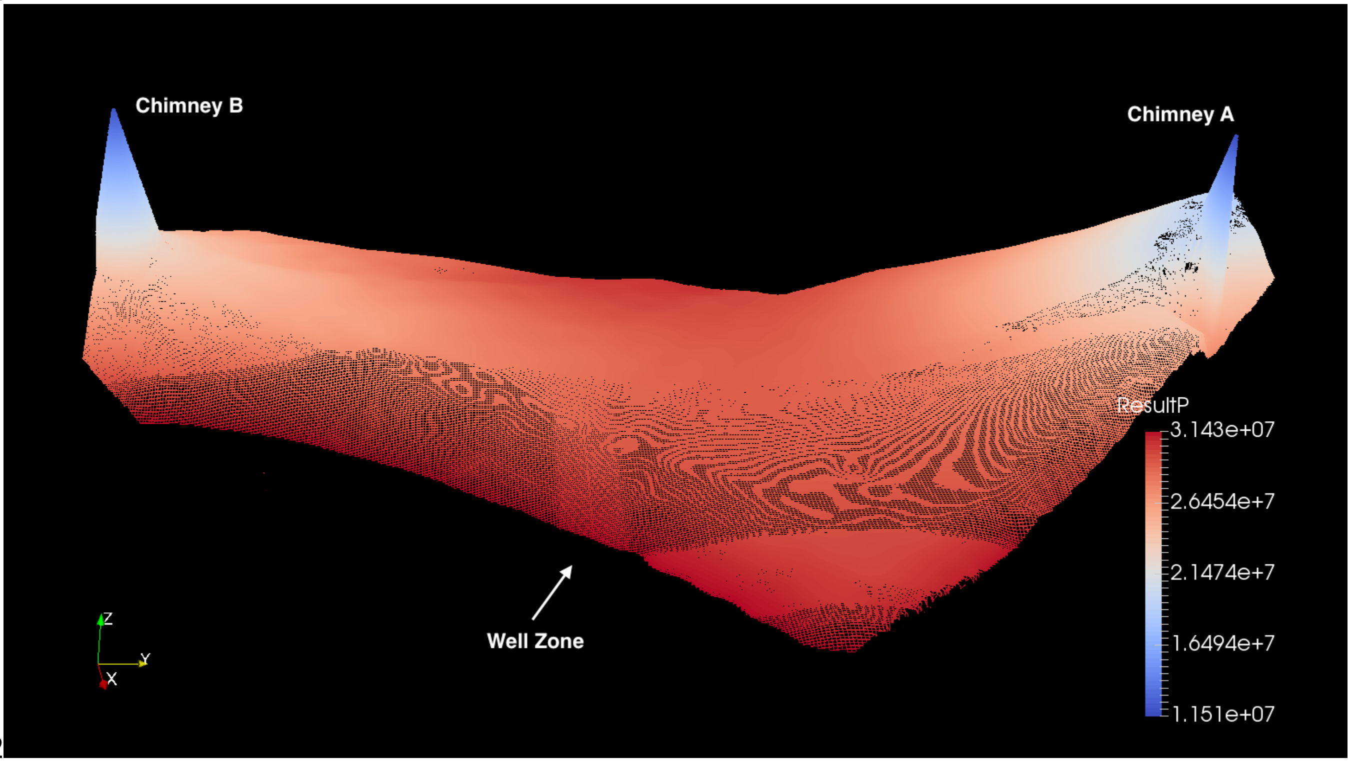

Figure 3. Grid connectivity and initial pressure distribution in the entire domain. “Well zone” points toward the region of the sand intersected by the well, and thus the point at which fluids from a failed casing shoe would emerge into the formation. Impermeable sediments overlying the sands are not visualized.

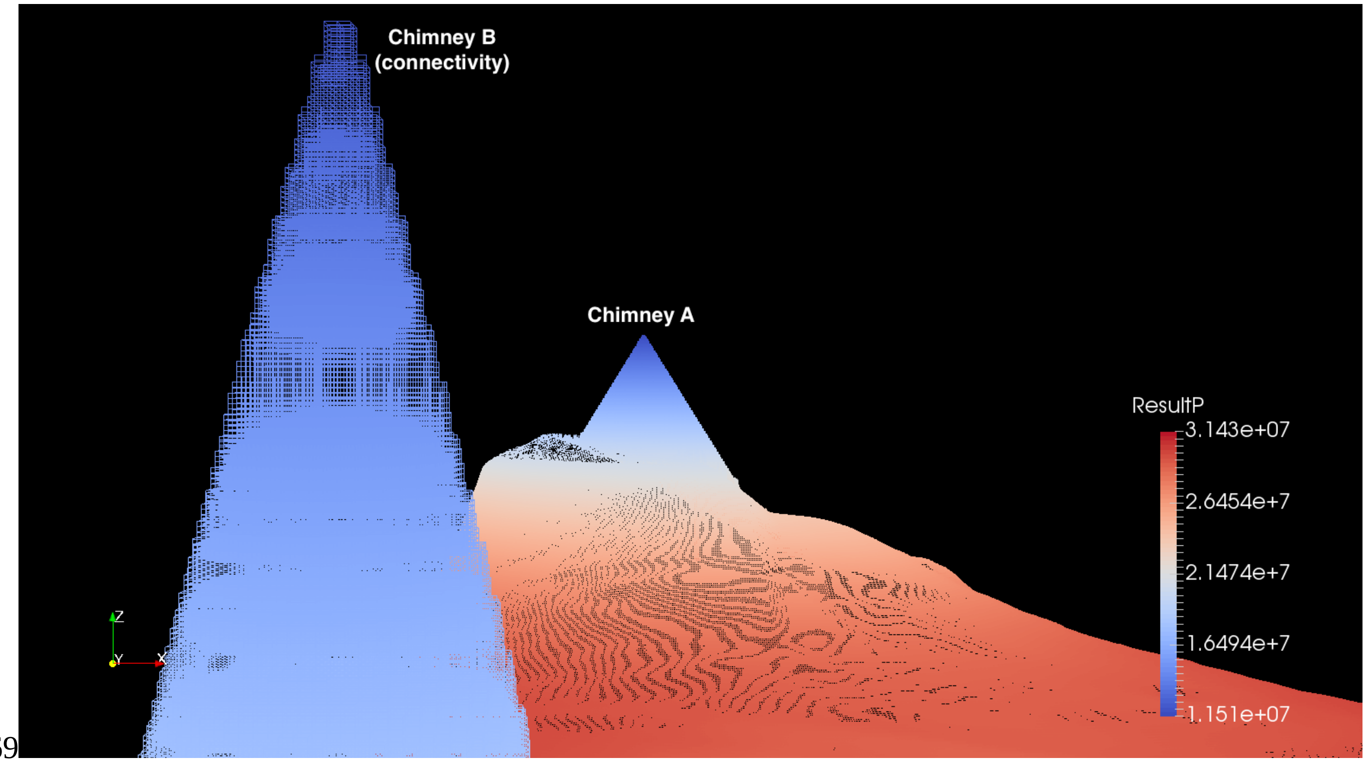

Figure 4. Connectivity and initial pressure distribution in the vicinity of Chimney B. Impermeable sediments overlying the sands are not visualized.

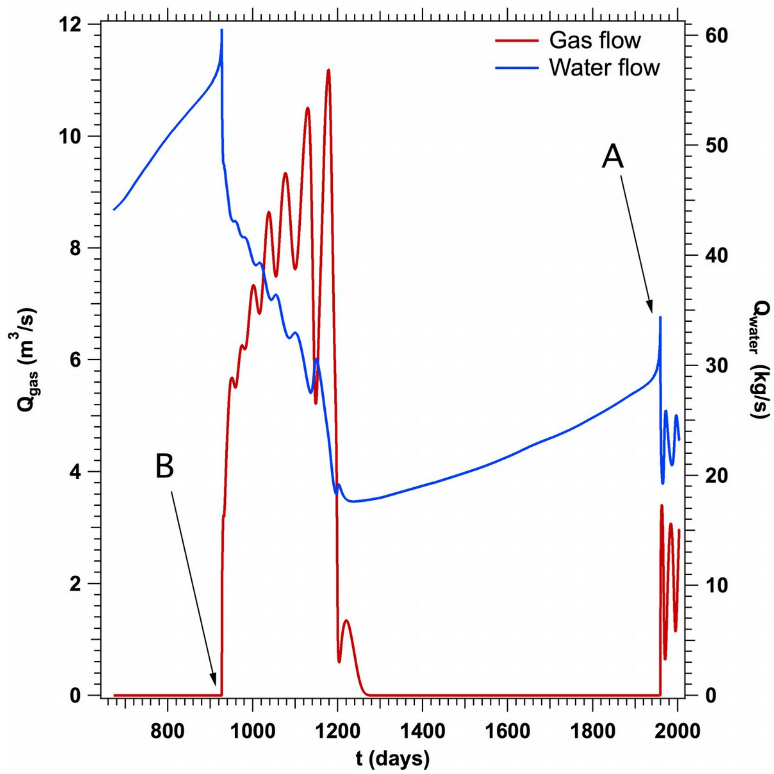

Figure 5: Gas and water flow rates at the seafloor (Chimney A + Chimney B) for the all-gas release case. Arrows indicate gas arrival times for Chimneys A and B.

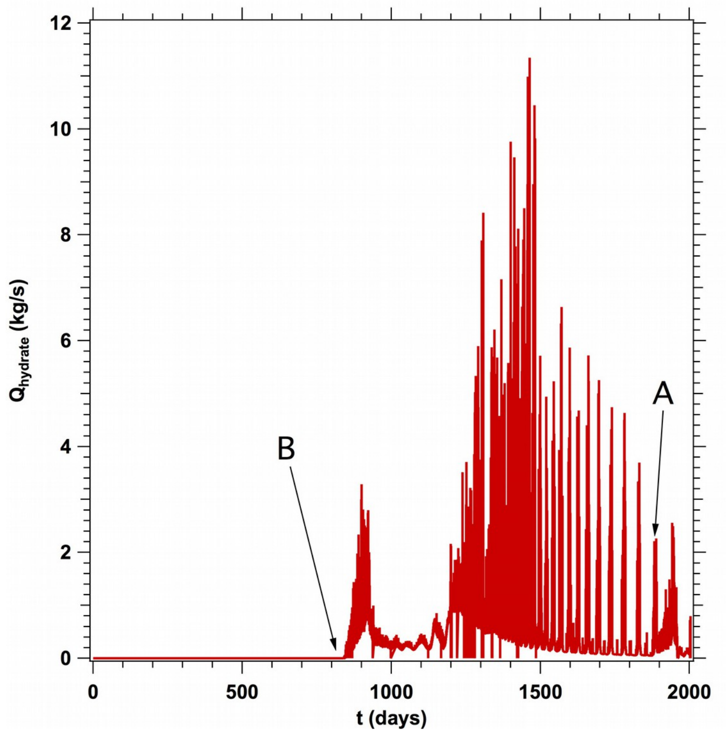

Figure 6: Total hydrate formation rate, Q_H, for the overall system for the all-gas release case.

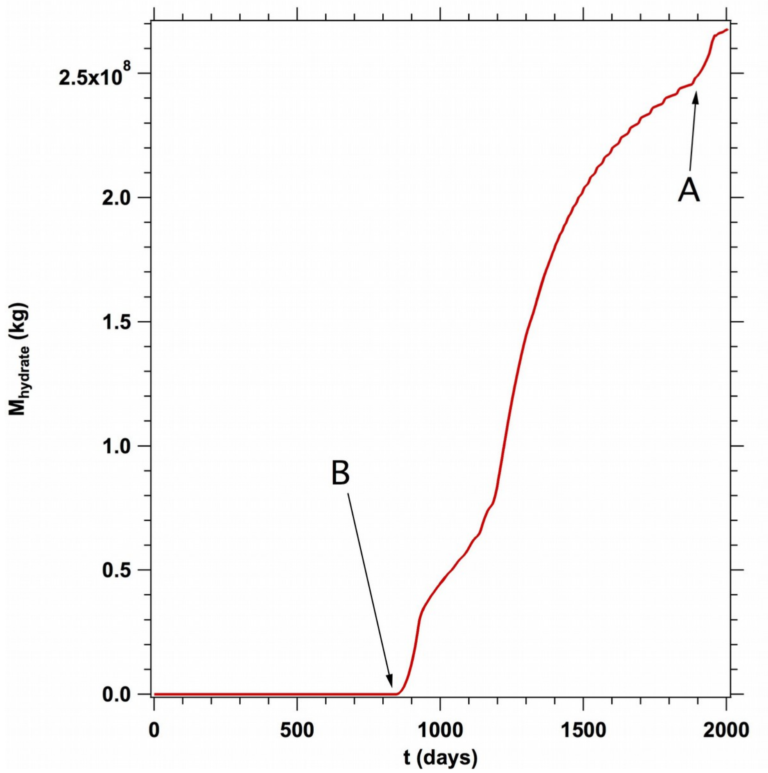

Figure 7: Cumulative hydrate formation, M_H, for the overall system in the all-gas release case.

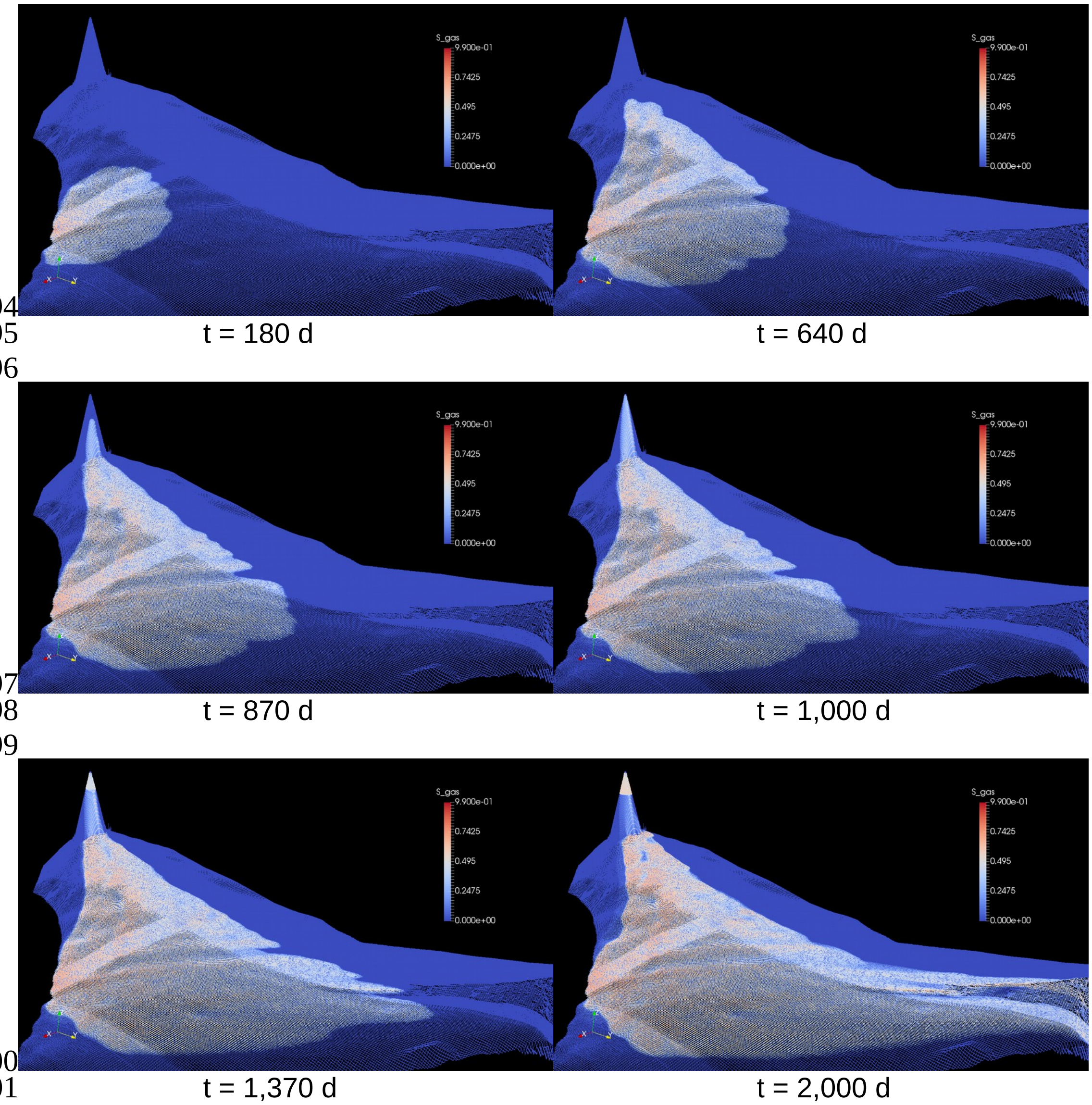

Figure 8: Visualizations of S_G, showing gas approach to, and release through, Chimney B.

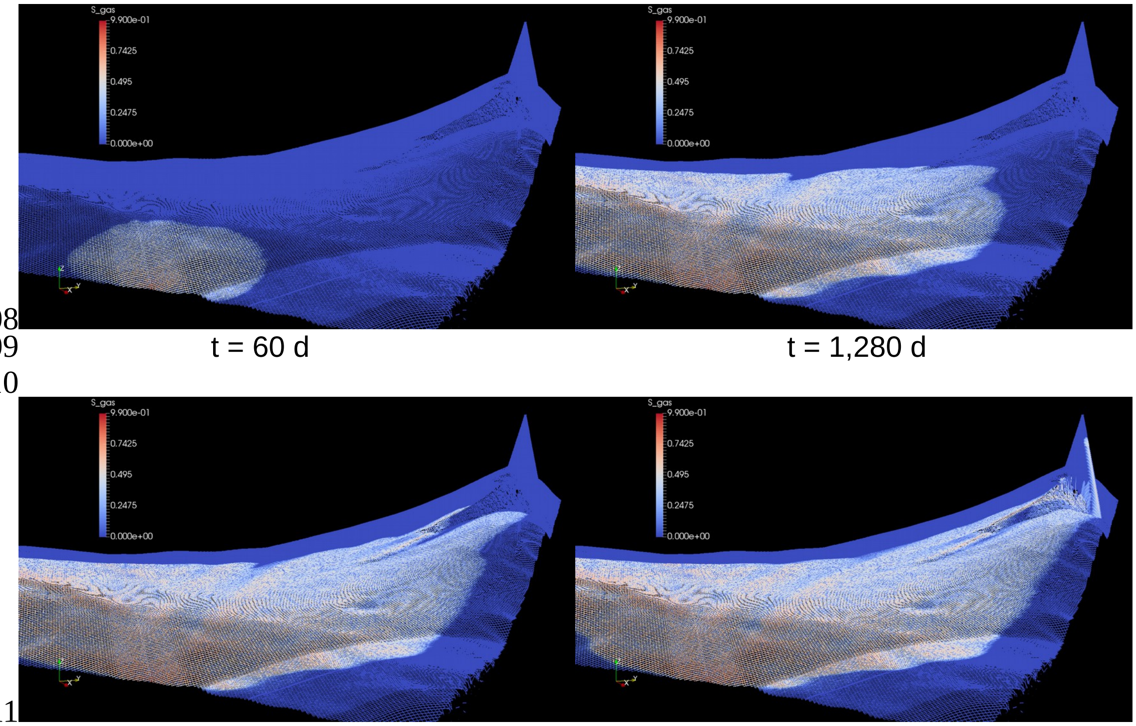

t = 60 d t = 1,280 d

t = 1,730 d t = 1,910 d

Figure 9: Visualizations of S_G, showing gas approach and release through Chimney A.

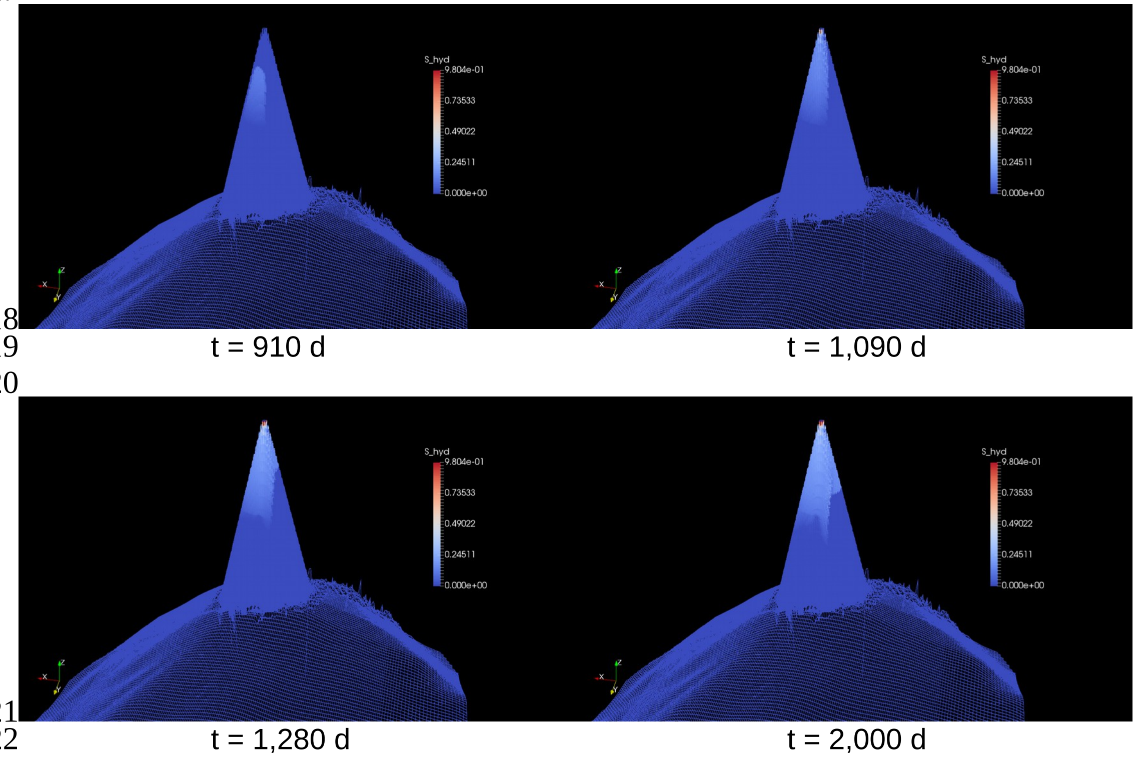

Figure 10: Visualizations of S_H, showing hydrate formation in Chimney B.

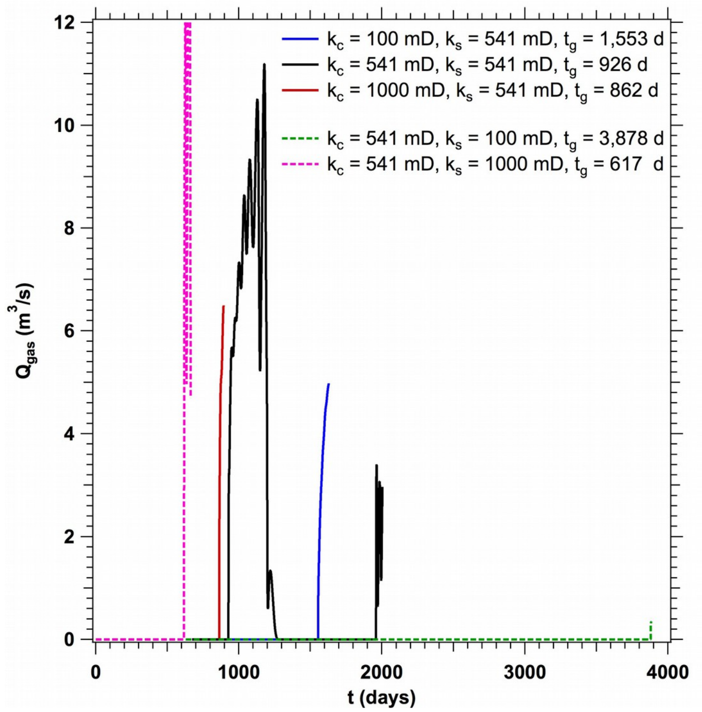

Figure 11: Variations in breakthrough curves, Q_G vs. t, as a function of permeabilities.

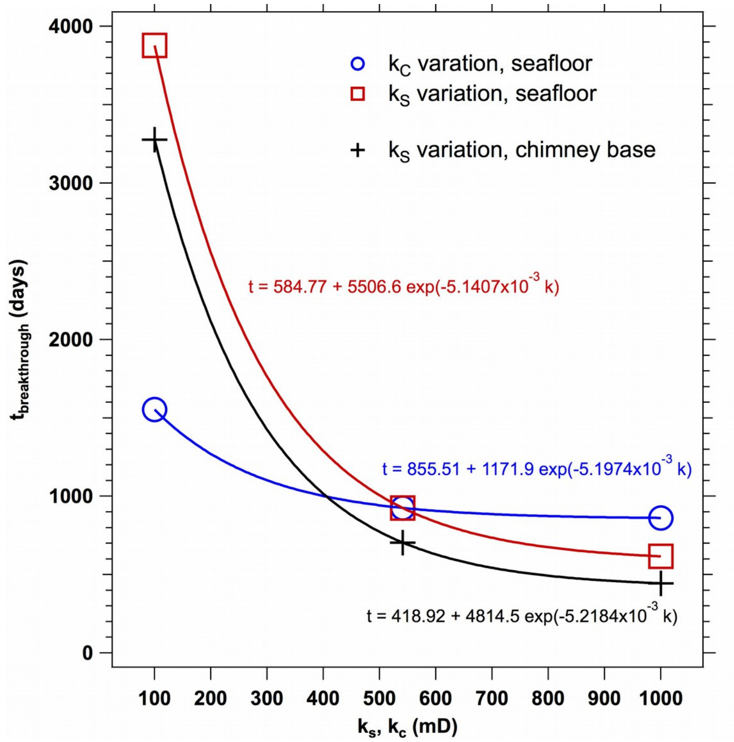

Figure 12: Gas arrival times at Chimney B and the seafloor as a function of permeabilities.

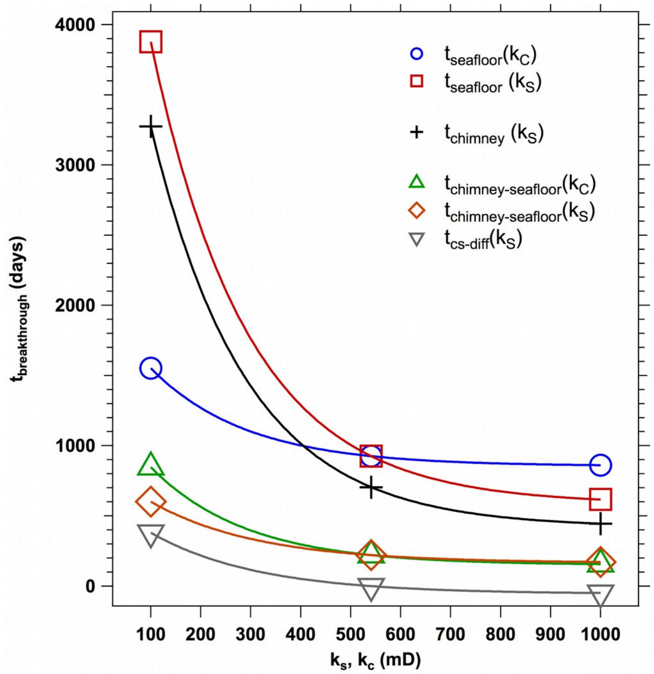

Figure 13: Gas arrival times at Chimney B and the seafloor, transit times through the chimney and k_s/k_c adjustment as a function of permeabilities.

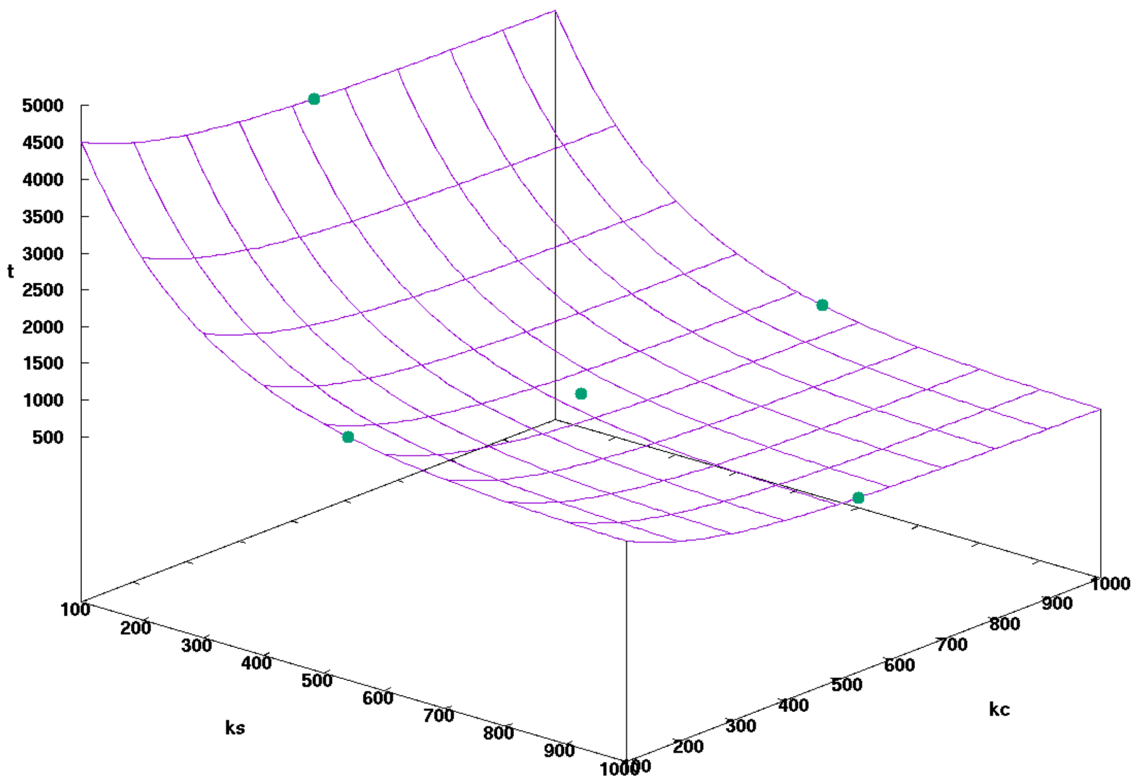

Figure 14: Gas arrival time surface as a function of k_S and k_C.

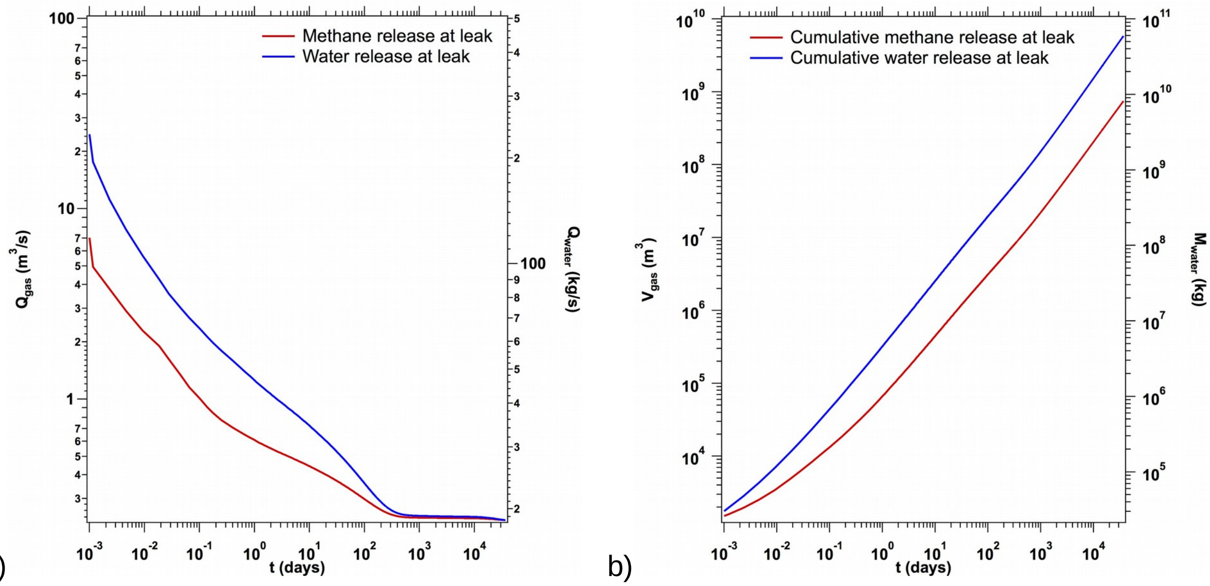

a) b)

Figure 15: Rates of water and gas released at the leak (a) and cumulative volume/mass (b).

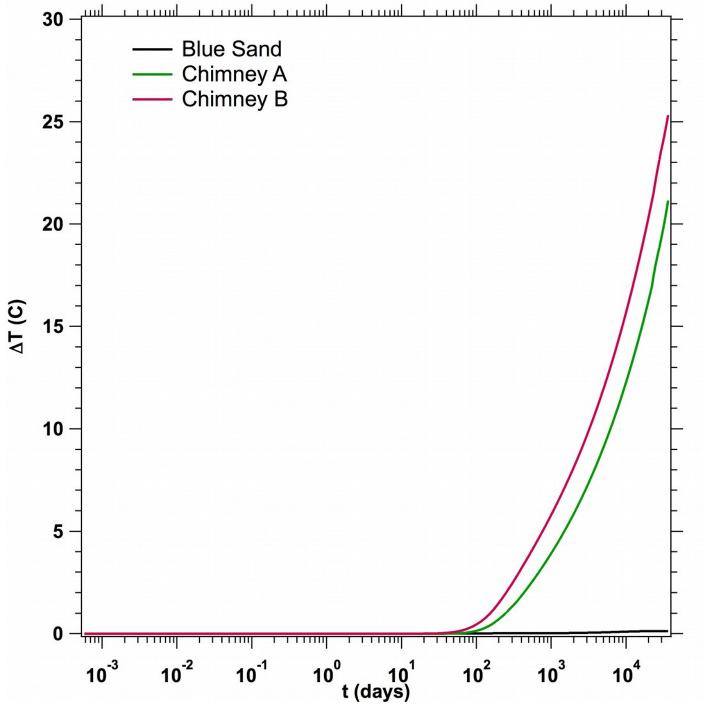

Figure 16: Change in temperature at monitoring points within the chimneys and in the Purple Sand

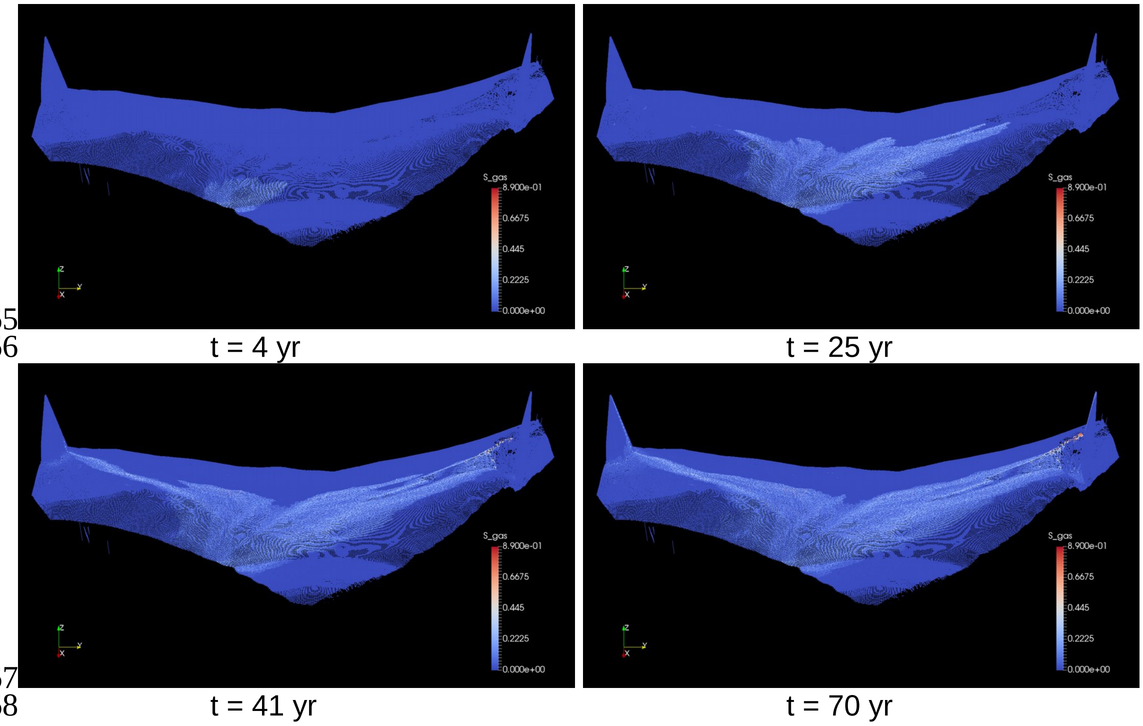

Figure 17: Visualizations of S_G, showing gas transport and escape through the chimneys for a mixture of water and gas.

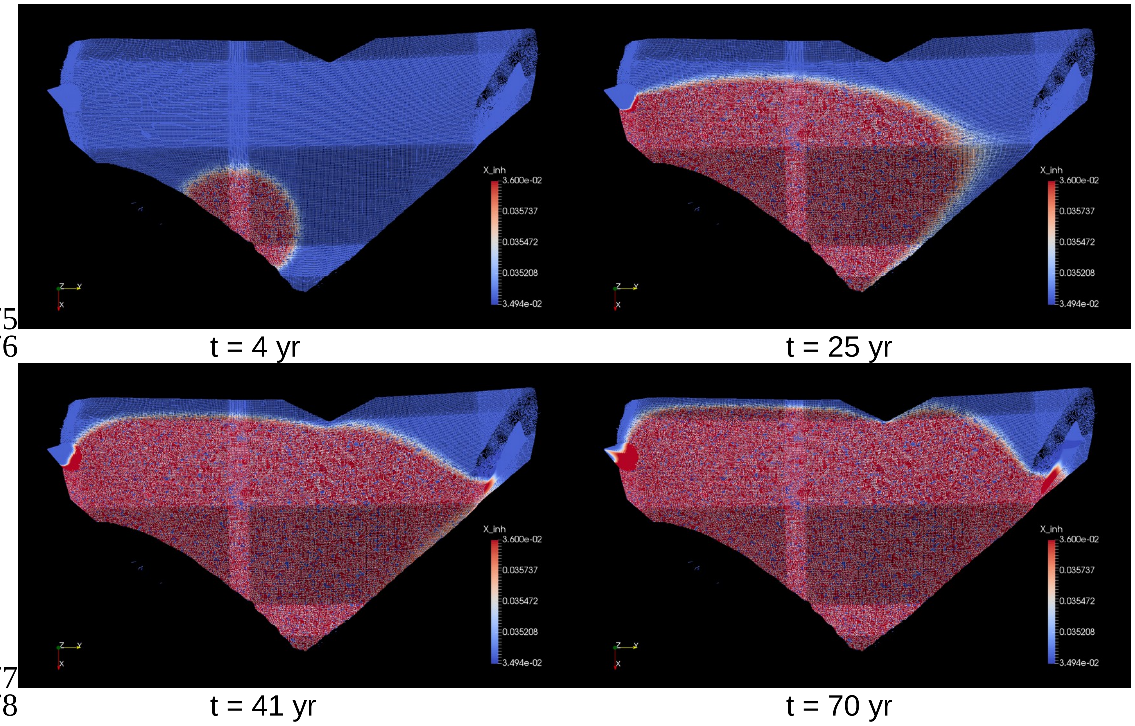

Figure 18: Visualizations of X_{NaCl}, showing brine transport and escape through the chimneys for a mixture of water and gas.